photonics

MDPI

Article

A Visible-to-Near-Infrared Broadband Dielectric-Based Metasurface Absorber with Resonant Coupling Cavity Effects

Fangzhou Chen *, Zhijian Huang, Zengsheng Huang and Shuo Wang

School of Astronautics, Nanjing University of Aeronautics and Astronautics, Nanjing 211106, China
* Correspondence: fchen1990@nuaa.edu.cn

Abstract

Dielectric-based metasurface absorbers have shown considerable potential in applications such as photodetection and solar energy harvesting. However, owing to the strict coupling conditions required to improve resonant absorption, achieving broadband absorption with dielectric-based metasurface absorbers remains challenging. In this study, a broadband absorber enhanced by metallic nanoparticles is proposed. The design is based on the near-field enhancement induced by localized surface plasmon resonance of nanoparticles and the Maxwell–Garnett theory. The structure employs Mie resonance and the Fabry–Pérot cavity effect of the Ge-SiO_2-Ge stack, along with the plasmonic effects of the doped layer and the TiN reflective layer, thereby facilitating high-efficiency absorption across the visible-to-near-infrared band (600–1020 nm), with an average absorptivity of 94.3%. The finite-difference time domain (FDTD) method is used to simulate how dimensional variations and different doping schemes influence the absorption spectra of the proposed metasurface absorber in the visible and short-wave near-infrared regions. The proposed absorber provides potential practical value for thermoelectric devices, infrared imaging and thermal detection applications.

Keywords: metasurfaces; Mie resonance; F-P cavity effect; nano metal doping; enhanced near-infrared absorption

1. Introduction

Against the backdrop of the global energy crisis and the rapid development of optoelectronic technologies, the efficient capture and conversion of natural electromagnetic energy have emerged as a key requirement for energy harvesting, high-sensitivity detection and radiation regulation [1]. Nevertheless, conventional materials are insufficient to achieve efficient broadband electromagnetic energy capture. Conversely, high-efficiency energy absorption is a prerequisite for improving energy conversion efficiency and system sensitivity. In recent years, perfect metamaterial and metasurface absorbers have undergone rapid development [2], owing to their superior wavefront manipulation and impedance matching capabilities, which have allowed them to overcome the performance limitations of traditional materials [3–5]. They have extensive application prospects in solar energy harvesting, high-performance optoelectronic detection and thermal radiation regulation. To fully exploit this potential, recent research has started incorporating intelligent optimization algorithms. For instance, Nipun et al. [6,7] demonstrated machine learning-optimized metamaterial absorbers that significantly improved design efficiency and broadband performance for solar energy harvesting and UV-to-infrared radiation shielding.

Check for updates

Received: 26 September 2026
Revised: 7 November 2026
Accepted: 12 November 2026
Published: 17 November 2026

Copyright: © 2026 by the authors. Licensee MDPI, Basel, Switzerland. This article is an open access article distributed under the terms and conditions of the Creative Commons Attribution (CC BY) license.

Dielectric-based metasurface perfect absorbers are more suitable for optoelectronic detection than traditional metal-based absorbers [8–11], primarily owing to their inherent mitigation of ohmic losses. Although a metallic back-reflector can effectively suppress transmission, achieving near-perfect absorption in such systems necessitates a precise balance between radiative and intrinsic material losses. This critical balance is typically realized by locally enhancing absorption through mechanisms such as dielectric electromagnetic resonances, critical coupling, and multipolar modes. Germanium (Ge) is characterized by extremely low ohmic loss and thermal emissivity, which render it a highly effective dielectric absorber for the near-infrared band [12,13]. Luo et al. proposed a single-layer Ge nanoantenna all-dielectric metasurface that exploits the coherent destructive interference between electric and magnetic dipole resonances in unit cells [14], which enables the structure to surpass the 50% absorption limit of traditional ultrathin films and achieve near-perfect absorption in the near-infrared region. However, limited by material dispersion and resonance coupling conditions, they were only able to achieve narrowband absorption.

Constructing multilayer structures is an effective strategy for expanding the absorption bandwidth of Ge-based metasurfaces [15,16]. For example, Zhang et al. proposed an ultra-broadband near-perfect absorber based on a single-layer Ge-assisted metasurface [17], in which the coupling and overlapping of multiple Mie resonances in the Ge nanoposts enable an average absorptivity of 96% over the 400–1300 nm band, which remains above 92% for incidence angles up to 50°. Nevertheless, such single-layer designs rely on carefully engineered resonance coupling, which limits further bandwidth extension. In parallel, recent efforts have explored ultrathin and polarization-independent configurations to achieve broadband absorption in the visible and infrared regions, such as the design proposed by Nipun et al. [7]. However, precisely balancing the resonant modes in such compact geometries remains a significant challenge. Therefore, to further boost light–matter interaction and overcome structural limitations, surface plasmonic effects have been introduced. These effects can excite intense localized electric fields around metallic nanoparticles, thereby enhancing light absorption in semiconductor and dielectric thin films [18,19]. To analyze the absorption performance of composite dielectrics, silver (Ag) nanoparticles are generally combined with the Maxwell–Garnett (MG) model or modified equivalent dielectric models [20,21].

Wang et al. proposed a high-performance infrared Ge-based plasmonic photodetector enhanced by a dual absorption mechanism [22], in which the localized surface plasmon resonance (LSPR) effectively offsets the low extinction coefficient and weak light absorption of pure Ge in the long-wavelength near-infrared band, substantially improving the near-infrared photoresponse. However, its resonance modes are heavily reliant on geometric parameters and material dispersion, and high-efficiency enhancement is achieved only within a narrow spectral window. Such a narrow effective bandwidth cannot satisfy the demands of broadband near-infrared detection. To compensate for the low extinction coefficient of Ge in the long-wavelength band, preserving high absorptivity requires precise tuning of structural thickness and geometric parameters. Similarly, the reduced extinction coefficient of silicon (Si) in the near-infrared region also leads to degraded absorption performance.

In recent years, resonance-hybridization approaches have provided an effective strategy for extending absorption bandwidths. For example, Nipun et al. [23]. demonstrated that a polarization-insensitive symmetric graphene metasurface can significantly enhance broadband near-unity absorption in the terahertz regime through the hybridization of surface and cavity plasmon resonances. Although the specific resonance mechanisms differ fundamentally, the underlying physical concept of multimode coupling is highly analogous. Consequently, our work leverages a similar hybridization philosophy, synergistically

combining Mie resonances, Fabry–Pérot (FP) cavity modes, and localized surface plasmon resonance (LSPR) from Ag nanoparticles to achieve broadband absorption.

Overall, dielectric materials exhibit weaker optical modulation capabilities than metals, which makes it difficult for dielectric-based metasurface systems to realize subwavelength ultrathin structures alongside ultra-broadband high-efficiency absorption [24,25]. Inspired by metallic nanoparticle doping technology [26,27], in the present study, a perfect absorber based on a three-layer Ge–SiO_2-Ge structure is introduced by combining the multilayer cavity structure with the diverse optical modulation modes of Ge metasurfaces [28]. The working principles and modulation mechanisms of different absorption modes are elucidated via theoretical analysis. Compared with previously reported designs, the proposed absorber achieves a competitive simulated absorptivity and shows potential for photodetection applications [29,30]. The permittivity of doped layers at various doping concentrations is calculated using equivalent medium theory, and the absorptivity of the structure is simulated across different wavelengths.

2. Materials and Methods

In the design of functional composite dielectrics, the equivalent medium theory is widely employed to rapidly calculate their equivalent electromagnetic parameters, which greatly improves the overall design efficiency. Equivalent medium theory is based on the following fundamental principle: when the size of inclusions in a dielectric is significantly smaller than the wavelength of incident light, the electromagnetic properties of the composite material can be analyzed macroscopically under the quasi-static approximation. For low inclusion concentrations with negligible inter-particle interactions and higher-order effects, the M-G theory can be adopted to compute the equivalent electromagnetic parameters of composite media [31,32]. Furthermore, existing experimental results have established that the M-G model is reliable when the filling factor is lower than 5%.

The inclusions are assumed to be spherical particles with radius R and permittivity ε_m. According to the Clausius–Mossotti equation, the relationship between particle polarizability α and the macroscopic permittivity ε_e of the particle-dielectric binary system can be expressed as follows:

$$\frac{\varepsilon_e - \varepsilon_h}{\varepsilon_e + 2\varepsilon_h} = \frac{n\alpha}{3\varepsilon_0} \tag{1}$$

where n and ε_h denote the number of particles per unit volume and the permittivity of the host dielectric, respectively. The polarizability is defined as follows:

$$\alpha = 4\pi\varepsilon_0 R^3 \frac{\varepsilon_m - \varepsilon_h}{\varepsilon_m + 2\varepsilon_h} \tag{2}$$

By substituting Equation (2) into Equation (1), the MG equivalent medium formula is obtained, where p represents the volume fraction of inclusions:

$$\frac{\varepsilon_e - \varepsilon_h}{\varepsilon_e + 2\varepsilon_h} = p\frac{\varepsilon_m - \varepsilon_h}{\varepsilon_m + 2\varepsilon_h} \tag{3}$$

After simplification, the following is produced:

$$\varepsilon_e = \varepsilon_h\left[1 - \frac{p}{\varepsilon_h/(\varepsilon_h - \varepsilon_m) - \frac{1}{3}(1-p)}\right] \tag{4}$$

The absorption performance of the absorber is simulated using the equivalent refractive index of the composite medium. In the present study, Ag nanoparticles are used with gradient doping concentrations of 0.25–1.25%, as illustrated in Figure 1.

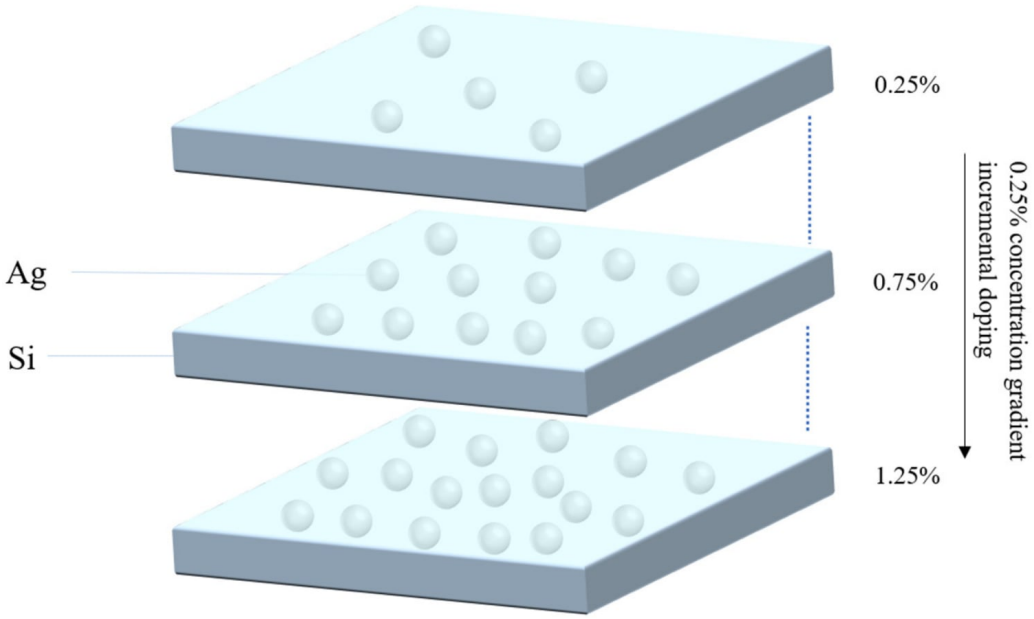


Figure 1. Schematic representation of the structure of a gradient-doped material.

Figure 2 illustrates the configuration of the proposed broadband absorber, which is a Ge–SiO_2–Ge stack fabricated on a doped silicon substrate. While the top Ge layer is composed of periodically arranged conical metasurface resonators, the other two layers are uniform thin films. The thickness parameters are as follows: H_1 = 450 nm, H_2 = 130 nm, H_3 = 70 nm and H_4 = 250 nm. As a reflecting mirror, the thickness of TiN is 100 nm. The total device thickness is 1000 nm. The doped layer in each film has a thickness of 50 nm. The period of the top Ge resonators is P = P_x = P_y = 600 nm, and the base side length is L = 400 nm.

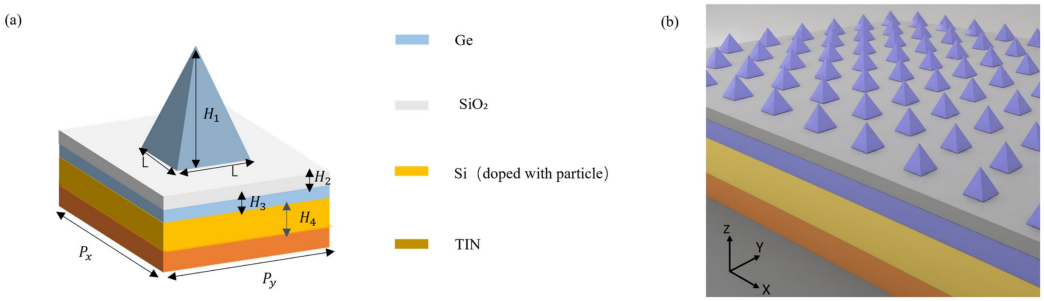


Figure 2. Structural schematic of the dielectric-based broadband metasurface absorber. (**a**) Three-dimensional model; (**b**) metasurface array.

We employ the finite-difference time domain (FDTD) method to simulate the performance of the metasurface absorber. The refractive indices of Ge and SiO_2 are adopted from Ciesielski et al. and Kischkat [33,34], and the data for silver particles and TiN comes from Johnson and palik, respectively. The proposed structure is polarization-insensitive. In the simulation, incident light is defined as a linearly polarized wave with the wave vector along the Z direction and the electric field along the X direction (TM polarization). Boundary conditions are defined as periodic boundaries along the X and Y axes, and perfectly matched layer along the Z axis, and the XYZ direction mesh is set to 10 nm to ensure the simulation's accuracy.

3. Results

The tapered top Ge layer fulfills the conditions for destructive interference. The three-layer structure forms a lossy FP cavity, with the resonant wavelength predicted by interference theory. When the reflected waves from two interfaces exhibit a phase difference of half a wavelength, destructive interference strongly suppresses reflection. This mechanism aligns with the phase-matching conditions of strong interference absorption, FP cavity absorption and cavity-coupled metasurface absorbers, as described by the following formula:

$$\delta = \frac{4\pi ndcos\theta}{\lambda} = (2m+1)\pi \quad (5)$$

where $nd = n_{SiO_2}H_2 + n_{Ge}(H_1 + H_3) \approx 2268.5$ nm represents the total effective optical path length of the Ge-SiO_2-Ge cavity. θ is the angle of incidence, λ is the wavelength, and m is an integer denoting the interference order. By substituting $m = 4$ and $m = 5$ into Equation (5), the theoretical resonances are predicted at 1008 nm and 825 nm, which closely align with the simulated absorption peaks λ_4 (990 nm) and λ_2 (815 nm), respectively. Minor deviations might come from the conical shape of the top Ge layer and the phase shift from lossy interfaces.

The enhanced absorption of the three-layer structure primarily arises from the resonant light trapping of the top conical Ge resonators, together with the cavity coupling effect between the top Ge layer and the bottom Ge film through the SiO_2 spacer. These combined effects intensify the local electric field inside the structure, elongate the effective optical path of light in Ge, and improve light absorption. Additionally, the doped layer enhances near-infrared absorption via the LSPR effect [35].

Figure 3a illustrates the spectral response of the proposed absorber. Absorptivity, $A(\lambda)$ is in terms of defined reflectance $R(\lambda)$ and transmittance $T(\lambda)$. The absorber achieves excellent broadband absorption across the visible-to-near-infrared (VIS-NIR) band, with an average absorptivity of 94.33% over 600–1020 nm and a peak absorptivity of 99.9% at 762 nm. Nearly perfect absorption is obtained in the 700–800 nm band, with an average absorptivity of 98.5% and an average reflectance of only 1.5%, which indicate excellent broadband antireflection performance. Notably, the decline in absorptivity beyond 1020 nm is caused by the reduced loss coefficient of Ge, resulting in higher reflectance.

The broadband absorption results from the combined influence of resonance modes excited by the top metasurface and the resonance of the multilayer thin-film cavity. To further elucidate the physical origin of the broadband absorption, we decomposed the absorber's structure and separately simulated the absorption performance of the structure without the doped layer and that of the SiO_2–Ge–TiN thin-film structure, with the corresponding absorption spectra shown in Figure 3b. To study the distribution of the absorption peaks, we extracted four characteristic peaks from the absorption spectrum of the combined structure (red curve) in Figure 3b and designated them as λ_1 to λ_4. When only the doped layer is removed, as indicated by the blue curve in Figure 3b, two pronounced absorption peaks appear at 815 nm and 900 nm, which coincide with the positions of λ_2 and λ_3, respectively. This result indicates that the resonant effects of the Ge metasurface primarily induce these two absorption modes, while the doped layer enables the structure to achieve near-perfect absorption in the 700–800 nm range. By contrast, when only the SiO_2–Ge–TiN film structure exists, as shown by the green curve, the average absorption across the 700–1000 nm range is approximately 55%. Although this broadband absorption effect arises from FP resonances within the few-layer film structure, the absence of the top metasurface compromises the antireflection condition, leading to a lower absorption efficiency compared to the composite structure.

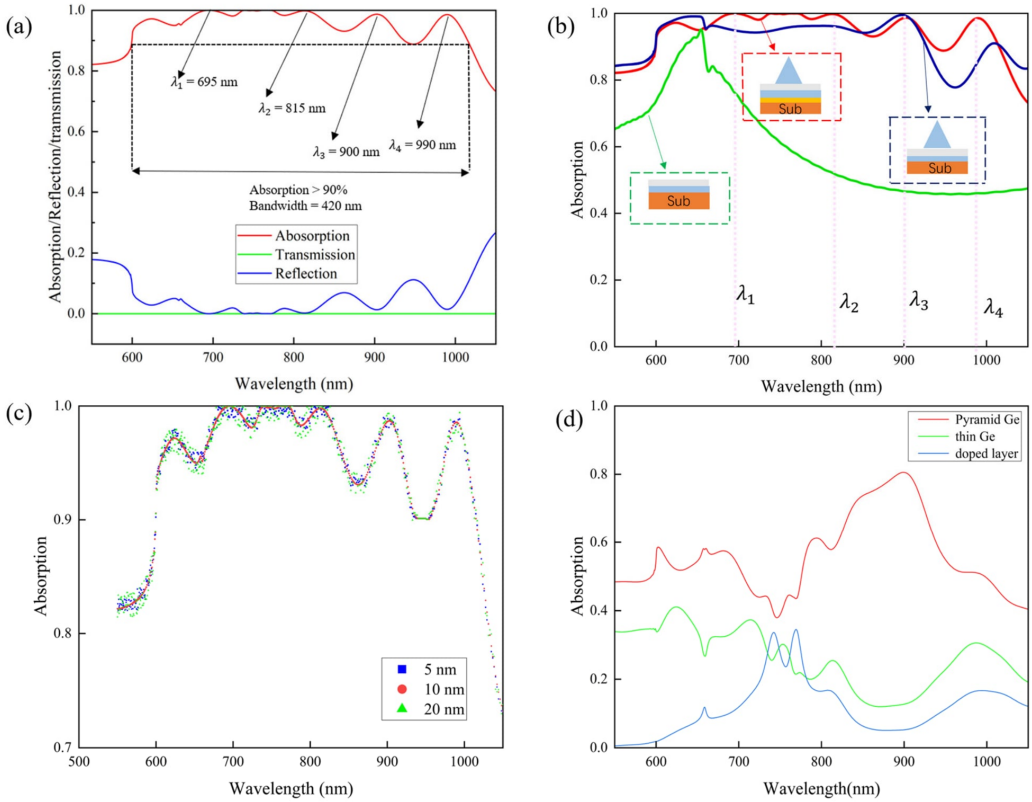


Figure 3. (**a**) Spectral response of the proposed absorber; (**b**) absorption spectra under various conditions (the structure color adhered from Figure 2); (**c**) absorption differences under different mesh precision; (**d**) the absorption of each layer in the composite structure.

To verify the numerical accuracy and elucidate the energy dissipation channels, Figure 3c,d present the mesh convergence analysis and layer-resolved absorption spectra, respectively. As shown in Figure 3c, the absorptivity spectra obtained under different mesh resolutions exhibit highly consistent trends. Specifically, the curves for the 5 nm and 10 nm meshes are almost identical, whereas a slight deviation is observed for the 20 nm mesh due to its lower computational resolution. This confirms that the 10 nm mesh adopted in this work is sufficiently converged to ensure simulation reliability. Figure 3d illustrates the absorption contributions from individual layers. It is clearly observed that the majority of the incident optical energy is confined and dissipated within the conical Ge and bottom Ge layers. Meanwhile, the doped layer exhibits a significant absorption enhancement within the 700–800 nm band, which is attributed to the strong localized surface plasmon resonance (LSPR) effect in this spectral region. TiN hardly absorbs any light when used as a mirror.

Based on the electric and magnetic field distributions illustrated in Figure 4, the correlation between resonance modes and structural design is further discussed. At $\lambda_1 = 695$ nm, the electric field is primarily concentrated at the side edges of the top Ge structure, and a periodically striped electric field distribution can be observed in the SiO_2 spacer and underlying regions. Such periodic variations in field intensity are characteristic of standing waves, confirming that an FP cavity is formed between the tapered Ge layer and the bottom doped Si/TiN layer. Incident light experiences multiple reflections and interferences between the upper and lower interfaces, thereby forming a stable standing wave inside the structure. In addition, local resonances in the top Ge layer strongly couple with vertical FP resonances.

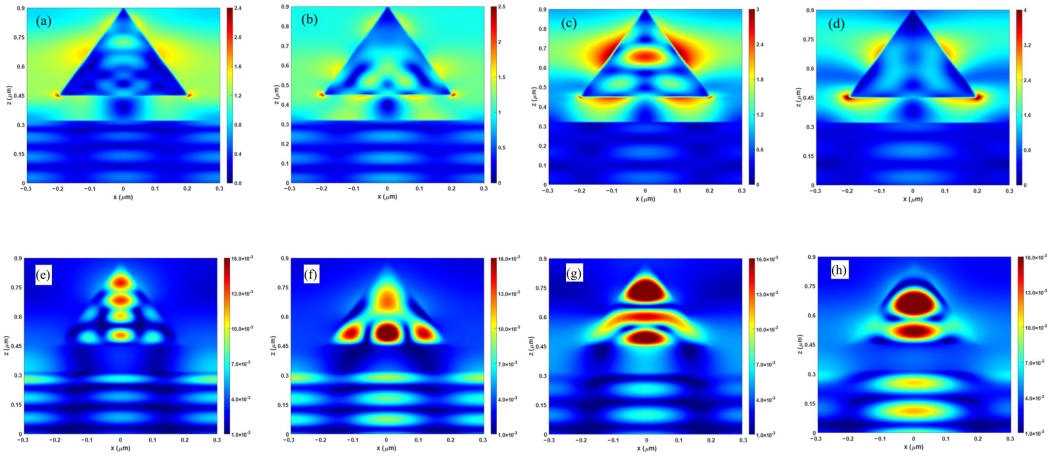


Figure 4. (**a**–**d**) Electric field distributions in the X–Z plane at 695, 815, 900, and 990 nm; (**e**–**h**) corresponding magnetic field distributions.

At λ_2 = 815 nm, the electric field is primarily concentrated at the base and edges of the conical Ge structure, which indicates that incident light is predominantly confined inside the structure. This phenomenon indicates that local resonant modes dominate at this wavelength, which results in a remarkable enhancement of the electric field within and at the edges of the structure. The FP cavity effect is especially pronounced in the underlying doped Si layer. At λ_3 = 900 nm, a noticeable high-field confinement region appears inside the conical Ge, leading to a strong localized electric field distribution. Light is effectively trapped within the cone, forming a localized resonance. Compared with the field distribution at 815 nm, electromagnetic energy is concentrated on the surface and stable modes are established inside the cone, which further improves optical field localization. Additionally, the doped Si layer generates localized plasmonic resonance. At λ_4 = 990 nm, the magnetic field distribution within dielectric layers shows that, owing to the coupling effects between LSPR and FP cavity modes, significant electric field enhancement occurs in the conical Ge, SiO_2 spacer, and underlying regions. Multimode coupling enables the multilayer structure to efficiently confine optical energy and support near-perfect absorption.

In summary, the absorption enhancement of the proposed structure is due to the coupling of multiple optical mechanisms. The tapered Ge layer attains efficient incident light coupling while generating localized electric field enhancement via its gradient geometry. The SiO_2 spacer forms an FP cavity between the upper and lower structures, thus extending the optical path length. Furthermore, the bottom Ge and doped Si layers provide scattering and energy dissipation pathways. When these modes are spectrally matched, these modes result in strong mode coupling, which leads to highly concentrated electric fields both within the structure and at interfacial regions. As a result, the absorber exhibits excellent absorption performance in the 600–1020 nm band.

To validate the rationale of the structural design, parameter selection and material configuration, the effects on absorption performance are systematically analyzed. The absorption characteristics of structures with doped layers under conditions of increased and reduced doping concentration are compared. Two comparative structures are established: Case 1 denotes the Ge–SiO_2–Ge structure without a doped layer, while Case 2 represents the structure with a reduced doping concentration. Figure 5a shows that the introduction of a doped layer markedly enhances the overall absorptivity in the 650–850 nm band. This can be attributed to the localized surface plasmon effects excited by Ag nanoparticles in the near-infrared region. Under incident light irradiation, free electrons in Ag nanoparticles undergo collective oscillation and form intense localized electric field hotspots on particle surfaces. Furthermore, light scattering induces slight fluctuations in the spectral curves,

and the equivalent refractive index of the doped layer increases with the rising doping concentration. As shown in Figure 5b, in the case of an increased doping concentration, the absorption curve of the structure with a reduced doping concentration exhibits a noticeable trough near 750 nm. For structures with an increased doping concentration, the design conforms to impedance matching theory, which is why the reflectance only shows minor fluctuations near the 760 nm band. On the contrary, the reflectance of the structure with a reduced doping concentration varies significantly, with a minimum value of 0.15 at 710 nm and a maximum value of 0.7 at 760 nm. The large variation in reflectance ultimately results in the emergence of absorption troughs.

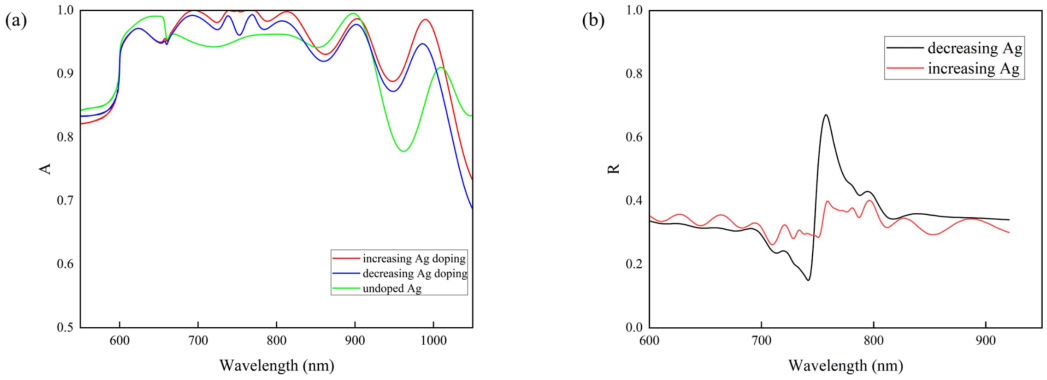


Figure 5. (**a**) Absorption spectra of the three structures; (**b**) reflectance curves of the isolated doped layers with different doping concentrations.

We also simulated the absorption performance under different structural parameters of the top cone. Figure 6a illustrates the influence of the structural parameters of the top conical Ge resonators on the absorber's performance. In Figure 6a, three vertical dashed lines are selected to indicate the characteristic frequencies for silicon-based detection (0.65 μm), short-wave optical communication (0.85 μm), and infrared sensing (0.94 μm). It can be observed that the absorptivity at 0.65 μm is comparable when H_1 is 0.45 μm and 0.5 μm. Meanwhile, a lower conical height leads to a significant decrease in absorptivity within the 0.85–0.94 μm range, because the Mie resonance and Fabry–Pérot resonance are suppressed, thereby reducing the average absorptivity. Furthermore, although the absorptivity at 0.94 μm for H_1 = 0.5 μm is slightly higher than that for H_1 = 0.45 μm, the difference is negligible, and a sharper cone is more difficult to fabricate.

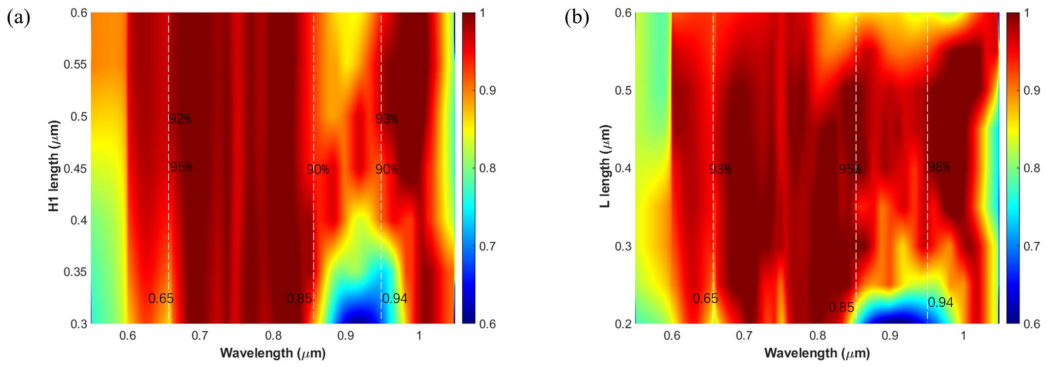


Figure 6. Absorption spectra obtained by varying (**a**) the height of the top-layer Ge and (**b**) the side length of the top Ge resonator.

In Figure 6b, variations in the base side length L of the cone also have a significant impact on the absorption characteristics. The parameter L determines the equivalent reflective

interface strength of the top layer, thereby further modulating the Fabry–Pérot (FP) cavity effect among the Ge–SiO_2–Ge layers. It can be seen that a lower L results in a noticeable decrease in absorptivity within the 0.85–0.94 μm range. An appropriate increase in L extends the effective optical path of the FP cavity, and the multi-beam interference and field enhancement effects between dielectric layers also vary with the value of L. As shown in Figure 6b, the absorptivity in the 0.65–0.94 μm range at $L = 0.4$ μm is slightly superior to that at $L = 0.5$ μm.

Therefore, by regulating the electromagnetic resonances, FP cavity effects, and impedance matching conditions, the structural parameters collectively determine the variations in absorption peaks, bandwidth, and average absorptivity. Based on global parameter optimization using FDTD simulations, the optimal structural dimensions are determined as $H_1 = 0.45$ μm and $L = 0.4$ μm, thereby achieving broadband and high-efficiency absorption.

Figure 7 illustrates the absorption spectra under different incident angles for TM and TE polarizations. The solid and dashed lines track the evolution trajectories of the main absorption peaks and the boundaries of the high-absorption region, respectively. Under oblique incidence, as the incident angle increases, due to the change in the effective refractive index and the in-plane wave vector component, the resonance modes at normal incidence exhibit a slight red-shift, causing the high-absorption region to shift accordingly (as indicated by the black lines). By contrast, in the mid-short wavelength band, the strong absorption effect of the multilayer structure, the FP cavity, compensates for the mode shift, resulting in minimal degradation of the absorption spectrum. However, it should be acknowledged that at larger incident angles, a localized decrease in absorptivity is observed in the long-wavelength region, with the minimum absorptivity dropping to approximately 80%. Despite this localized drop, the overall broadband absorption remains highly robust. The band-averaged absorptivity across the 600–1020 nm range remains highly robust at 88% for TE and 92% for TM polarization.

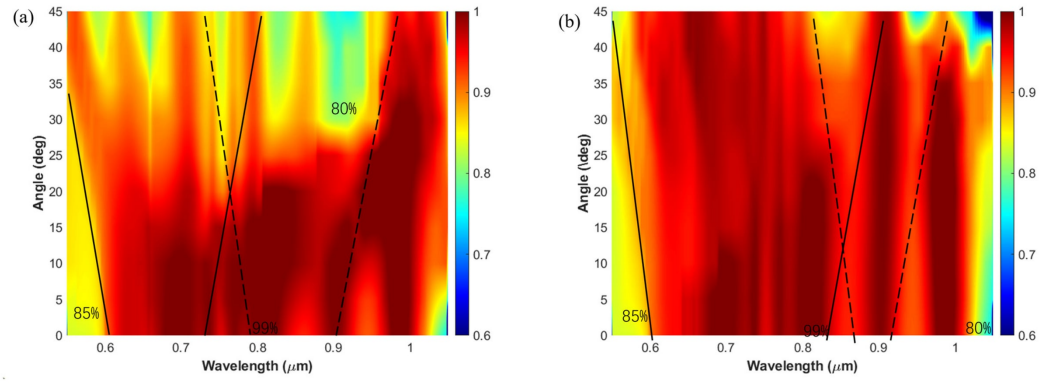


Figure 7. (**a**) Schematic diagram of absorption under TE polarization; (**b**) schematic diagram of absorption under TM polarization.

To place the current study in the context of recent developments, Table 1 summarizes several representative studies. These works utilize various material systems to broaden the absorption bandwidth or enhance angular stability. In contrast to Zhang et al. [15], who rely on strict Mie resonance coupling within a single pure Ge layer, or all-dielectric designs like Yang et al. [11], the present study maintains a dielectric-based multilayer architecture with gradient Ag doping. As shown in the table, while our average absorptivity (94.3%) and angular stability (45°) are competitive, our design achieves an exceptional peak absorptivity of 99.9% at 762 nm.

Table 1. Comparison of the proposed absorber with recent broadband absorbers.

Literature	Operating Wavelength	Avg. Absorption	Angular Stability	Ultimate Absorption Rate	Design/Optimization Approach	Fabrication Complexity
Zhang et al. [15]	400–1300 nm	96%	50° (average 92%)	N/A	Pure Mie resonance; geometric tuning	High (requires deep Ge etching)
Xiong et al. [16]	NIR	>70%	N/A	>70%	Elliptical nanohole array	Medium (multilayer)
Yang et al. [11]	330–700 nm	93.9%	N/A	97.3%	Cavity coupling; geometric tuning	Medium (all-dielectric)
This Work	600–1020 nm	94.3%	45° (92% for TM 88% for TE)	99.9%	Mie-FP-LSPR synergy; Material-level gradient doping	Medium (dielectric-based multilayer)

It should be noted that the performance metrics reported in Table 1 should not be interpreted as a direct performance ranking. The compared studies employ different material systems (e.g., pure Ge single-layers vs. multilayer dielectric stacks) and distinct resonance mechanisms (e.g., localized Mie resonances vs. hybrid Fabry–Pérot and plasmonic coupling). Furthermore, different evaluation criteria are often used to define the "operating bandwidth" (e.g., absorptivity >90% vs. 3 dB bandwidth). Therefore, the absorptivity and bandwidth metrics in this study, which are obtained based on an idealized loss model in FDTD simulations, are not directly equivalent to those in studies where performance may be influenced by non-ideal experimental conditions or different normalization standards. This comparison primarily aims to highlight the differences in design mechanisms, structural degrees of freedom, and fabrication complexity, rather than to establish a universal absorptivity ranking.

4. Discussion

In the present work, the performance of a Ge–SiO_2–Ge–Si(Ag) is simulated and analyzed. By integrating the FP cavity effects of the dielectric stack with the localized plasmonic effects of Ag nanoparticles and the TiN reflective layer, the dielectric-based structure achieves broadband high-efficiency absorption. The average absorptivity reaches 94.3% in the 600–1020 nm wavelength range. Furthermore, the angle insensitivity and polarization independence of the absorber are verified. The electromagnetic field distributions at four resonance peaks are analyzed to reveal the physical mechanism of broadband absorption. In addition, parameter sweeping simulations are conducted to optimize the structural design, and the influences of microstructure and material configuration on absorption performance are explored. The proposed device exhibits potential value for application in optoelectronic photodetectors and related systems. While the current study focuses on passive broadband absorption, future developments could incorporate active materials for dynamic tuning. For example, thermally switchable absorbers based on phase-change materials like VO_2 have been demonstrated in the terahertz regime by Nipun et al. [36]. Therefore, integrating such active mechanisms into our dielectric-based VIS-NIR platform could enable reconfigurable photodetection and further expand its practical applicability.

Author Contributions: Conceptualization, F.C.; methodology, F.C.; validation, F.C. and Z.H. (Zhijian Huang); formal analysis, Z.H. (Zhijian Huang); investigation, Z.H. (Zhijian Huang) and S.W.; resources, Z.H. (Zhijian Huang); data curation, Z.H. (Zhijian Huang); writing—original draft preparation, Z.H. (Zhijian Huang); writing—review and editing, F.C.; visualization, Z.H. (Zhijian Huang) and Z.H. (Zengsheng Huang); supervision, F.C.; project administration, F.C. All authors have read and agreed to the published version of the manuscript.

Funding: This research received no external funding.

Data Availability Statement: The data underlying the results presented in this paper are not publicly available at this time but may be obtained from the authors upon reasonable request.

Conflicts of Interest: The authors declare no conflicts of interest.

References

1. Wu, L.; Chen, X.; Zhang, D. Iron-only Metasurface Broadband absorber for solar energy harvesting. *Nanomaterials* **2025**, *15*, 1263. [CrossRef] [PubMed]
2. Wang, B.-X.; Xu, C.; Duan, G.; Xu, W.; Pi, F. Review of Broadband Metamaterial Absorbers: From Principles, Design Strategies, and Tunable Properties to Functional Applications. *Adv. Funct. Mater.* **2023**, *33*, 2213818. [CrossRef]
3. Hayat, B.; Zhang, J.; Khan, A.; Abbas, S.M.; Majeed, A.; Al-Bawri, S.S. A flexible and optical transparent Metasurface absorber with broadband RCS reduction characteristics. *Nanomaterials* **2024**, *14*, 1507. [CrossRef] [PubMed]
4. Kim, Y.; Lee, J.-H. Broadband Metasurface Absorber based on an optimal combination of copper tiles and chip resistors. *Materials* **2023**, *16*, 2692. [CrossRef] [PubMed]
5. Samal, P.K.; Sahu, S.; Behera, G. Design of tunable perfect absorber based on vanadium dioxide Metasurface for sensing applications. *Optik* **2024**, *311*, 171878. [CrossRef]
6. Nipun, M.M.K.; Rana, S.M.R.; Morshed, M.G.; Amin, K.M.; Ahamed, F.S.; Khan, H.F. Broadband Solar Energy Harvesting with a Machine-Learning-Optimized Nickel–Quartz Metamaterial Absorber. *J. Nanophotonics* **2025**, *19*, 046003. [CrossRef]
7. Nipun, M.M.K.; Rana, S.M.R.; Morshed, M.G.; Jahan, I.; Ahamed, F.A.S. Machine Learning-Driven Metamaterial Absorbers for Solar Energy Harvesting and UV to Infrared Radiation Shielding. *J. Sci. Adv. Mater. Devices* **2026**, *11*, 101172. [CrossRef]
8. Grayli, S.V.; Patel, T.; van Kasteren, B.; Kokilathasan, S.; Tekcan, B.; Tam, M.C.A.; Losin, W.F.; Odinotski, S.; Tsen, A.W.; Wasilewski, Z.R.; et al. Near-unity Absorption in semiconductor Metasurfaces using Kerker interference. *Nano Lett.* **2025**, *25*, 9362–9368. [CrossRef] [PubMed]
9. Zhang, W.; Sun, G.; Wei, J.; Miao, Y.; Fan, R.; Wang, Q.; Chen, Y. A broadband long-wavelength infrared all-dielectric Metasurface absorber based on Mie resonance. *Nanoscale* **2025**, *17*, 18834–18842. [CrossRef] [PubMed]
10. Ge, J.; Gao, Y.; Xu, L.; Zhou, N.; Shen, X. Dual-symmetry-perturbed all-dielectric resonant Metasurfaces for high-Q perfect light absorption. *Chin. Opt. Lett.* **2024**, *22*, 023602. [CrossRef]
11. Yang, F.; Shi, X.; Wu, Z.; Guo, S.; Wei, X.; Jiang, J.; Geng, J.; Zhu, S.; Xu, H.; Liang, Z. Ultra-thin UV–visible all-dielectric broadband metasurface absorber with resonant coupling of cavity effect. *Opt. Lett.* **2025**, *50*, 6028. [CrossRef] [PubMed]
12. Ye, M.-J.; Bikbaev, R.G.; Maksimov, D.N.; Pankin, P.S.; Kim, M.; Timofeev, I.V.; Chen, K.-P. Germanium metasurface near-infrared high-q absorber with symmetry-protected bound states in the continuum. *Chin. J. Phys.* **2024**, *92*, 188–194. [CrossRef]
13. Cai, B.; Wu, L.; Zhu, X.; Cheng, Z.; Cheng, Y. Ultra-broadband and wide-angle plasmonic light absorber based on all-dielectric gallium arsenide (GaAs) metasurface in visible and near-infrared region. *Results Phys.* **2024**, *58*, 107509. [CrossRef]
14. Tian, J.; Luo, H.; Li, Q.; Pei, X.; Du, K.; Qiu, M. Near-infrared Super-Absorbing All-Dielectric Metasurface based on single-layer germanium nanostructures. *Laser Photonics Rev.* **2018**, *12*, 1800076. [CrossRef]
15. Zhao, J.; Wang, Y.; Zhu, Y.; Zhang, W.; Yu, Y. Lithography-free flexible perfect broadband absorber in visible light based on an all-dielectric multilayer structure. *Opt. Lett.* **2020**, *45*, 5464. [CrossRef] [PubMed]
16. Xiong, Q.; Yu, H.; Zhang, Y.; Gao, X.; Chen, C. Broadband near infrared all-dielectric Metasurface absorber. *Results Phys.* **2021**, *30*, 104813. [CrossRef]
17. Zhang, H.; Wu, K. Ultra-broadband near-perfect absorber based on a single-layer Ge-assisted Metasurface. *J. Opt. Soc. Am. B* **2022**, *39*, 332. [CrossRef]
18. Su, J.; Hou, X.; Dai, N.; Li, Y. Localized surface plasmon resonance enhanced photodetector: Physical model, enhanced mechanism and applications. *Front. Phys.* **2024**, *19*, 63501. [CrossRef]
19. Kaur, H.J. Investigation of germanium-based plasmonic-photo-detector improved by dual-absorption method using titanium nitride. *J. Opt.* **2023**, *52*, 1818–1825. [CrossRef]
20. Maurice, M.S.; Barros, N.; Kachkachi, H. Beyond the Maxwell Garnett approximation for interacting plasmonic nanoparticles: An analytical and numerical study. *J. Appl. Phys.* **2023**, *134*, 094303. [CrossRef]
21. García-Valenzuela, A.; Acevedo-Barrera, A.; Vázquez-Estrada, O.; Nahmad-Rohen, A.; Barrera, R.G. Full dynamic corrections to the Maxwell Garnett mixing formula and corresponding extensions beyond the dipolar approximation. *J. Quant. Spectrosc. Radiat. Transf.* **2023**, *302*, 108578. [CrossRef]
22. Wang, L.; Zhang, Y.; Wang, B.; Wei, Y.; Zhang, B.; Meng, L.; Liu, T.; Wang, B.; Han, B.; Jiang, Z.; et al. High-performance infrared Ge-based plasmonic photodetector enhanced by dual absorption mechanism. *APL Photonics* **2020**, *5*, 096104. [CrossRef]
23. Nipun, M.M.K.; Islam, M.J.; Sultana, T. Numerical Investigation of Broadband Near-Unity Terahertz Absorption Using a Polarization-Insensitive Symmetric Graphene Metasurface. *J. Sci. Adv. Mater. Devices* **2026**, *11*, 101246. [CrossRef]

24. Zografopoulos, D.C.; Tsilipakos, O. Recent advances in strongly resonant and gradient all-dielectric metasurfaces. *Mater. Adv.* **2023**, *4*, 11–34. [CrossRef]
25. Barati Sedeh, H.; Litchinitser, N.M. From non-scattering to super-scattering with Mie-tronics. *Photonics Res.* **2024**, *12*, 608. [CrossRef]
26. Chong, H.; Mu, Y.; Cai, Y.; Ye, H. Tailored absorption/emission and ultrastrong coupling from heavily doped germanium plasmonic antennas. *Opt. Laser Technol.* **2024**, *175*, 110731. [CrossRef]
27. Salem, M.; Boussaid, A.; Ben Hamida, M.B. Opto-Electronic roperties Enhancement of silicon solar cells by iron doped ZnO nanoparticles. *Silicon* **2023**, *15*, 3543–3548. [CrossRef]
28. Xu, R.; Morimoto, T.; Takahara, J. Vertical photon sorting by stacking silicon and germanium nanopillars for broadband absorbers. *Nanophotonics* **2023**, *12*, 2461–2469. [CrossRef] [PubMed]
29. Zhou, Z.-X.; Ye, M.-J.; Yu, M.-W.; Yang, J.-H.; Su, K.-L.; Yang, C.-C.; Lin, C.-Y.; Babicheva, V.E.; Timofeev, I.V.; Chen, K.-P. Germanium Metasurfaces with Lattice Kerker Effect in near-infrared photodetectors. *ACS Nano* **2022**, *16*, 5994–6001. [CrossRef] [PubMed]
30. Yezekyan, T.; Zenin, V.A.; Thomaschewski, M.; Malureanu, R.; Bozhevolnyi, S.I. Germanium Metasurface assisted broadband detectors. *Nanophotonics* **2023**, *12*, 2171–2177. [CrossRef] [PubMed]
31. Markel, V.A. Introduction to the Maxwell Garnett approximation: Tutorial. *J. Opt. Soc. Am. A* **2016**, *33*, 1244. [CrossRef] [PubMed]
32. Fedorov, A.S.; Eremkin, E.V. Charge transfer plasmons in nanoparticle arrays on graphene: Theoretical development. *J. Appl. Phys.* **2024**, *136*, 043101. [CrossRef]
33. Ciesielski, A.; Skowronski, L.; Pacuski, W.; Szoplik, T. Permittivity of Ge, Te and Se thin films in the 200–1500 nm spectral range. Predicting the segregation effects in silver. *Mater. Sci. Semicond. Process.* **2018**, *81*, 64–67. [CrossRef]
34. Kischkat, J.; Peters, S.; Gruska, B.; Semtsiv, M.; Chashnikova, M.; Klinkmüller, M.; Fedosenko, O.; Machulik, S.; Aleksandrova, A.; Monastyrskyi, G.; et al. Mid-infrared optical properties of thin films of aluminum oxide, titanium dioxide, silicon dioxide, aluminum nitride, and silicon nitride. *Appl. Opt.* **2012**, *51*, 6789. [CrossRef] [PubMed]
35. Sun, Y.; Chen, F.; Li, X. Silicon based near-infrared absorption enhancement structure with gradient doping of nano metal particles. *Infrared Laser Eng.* **2024**, *53*, 20230519.
36. Nipun, M.M.K.; Islam, M.J. Thermally Switchable Broadband Terahertz Metamaterial Absorber Based on VO_2 for Low-Reflection Absorptive Shielding. *Phys. Status Solidi A* **2026**, *223*, 70528. [CrossRef]

Disclaimer/Publisher's Note: The statements, opinions and data contained in all publications are solely those of the individual author(s) and contributor(s) and not of MDPI and/or the editor(s). MDPI and/or the editor(s) disclaim responsibility for any injury to people or property resulting from any ideas, methods, instructions or products referred to in the content.